ADVANCED ENERGY MATERIALS
www.advenergymat.de

Accelerated Perovskite Oxide Development for Thermochemical Energy Storage by a High-Throughput Combinatorial Approach

*Runxia Cai, Hilal Bektas, Xijun Wang, Kyle McClintock, Lauren Teague, Kunran Yang, and Fanxing Li**

The structural and compositional flexibility of perovskite oxides and their complex yet tunable redox properties offer unique optimization opportunities for thermochemical energy storage (TCES). To improve the relatively inefficient and empirical-based approaches, a high-throughput combinatorial approach for accelerated development and optimization of perovskite oxides for TCES is reported here. Specifically, thermodynamic-based screening criteria are applied to the high-throughput density functional theory (DFT) simulation results of over 2000 A/B-site doped $SrFeO_{3-\delta}$. 61 promising TCES candidates are selected based on the DFT prediction. Of these, 45 materials with pure perovskite phases are thoroughly evaluated. The experimental results support the effectiveness of the high-throughput approach in determining both the oxygen capacity and the oxidation enthalpy of the perovskite oxides. Many of the screened materials exhibit promising performance under practical operating conditions: $Sr_{0.875}Ba_{0.125}FeO_{3-\delta}$ exhibits a chemical energy storage density of 85 kJ kg_{ABO3}^{-1} under an isobaric condition (with air) between 400 and 800 °C whereas $Sr_{0.125}Ca_{0.875}Fe_{0.25}Mn_{0.75}O_{3-\delta}$ demonstrates an energy density of 157 kJ kg_{ABO3}^{-1} between 400 °C/0.2 atm O_2 and 1100 °C/0.01 atm O_2. An improved set of optimization criteria is also developed, based on a combination of DFT and experimental results, to improve the effectiveness for accelerated development of redox-active perovskite oxides.

1. Introduction

The urgent need to mitigate global warming requires a swift reduction in CO_2 emissions from fossil fuel utilization.[1] As such, promising technologies that can reduce our reliance on fossil fuels and accelerate the shift toward renewable energy are highly desirable.[2] The intermittent nature of renewable electricity generated from wind and solar requires considerable compensation from other energy sources, limiting their shares in the power grid.[3–6] Therefore, energy storage systems, which reduce the temporal and spatial imbalances between electricity generation and consumption, will play a critical role in accelerating the renewable transition.[7]

Various energy storage approaches have been proposed to store different forms of energy, such as pumped hydro, batteries, compressed air, flywheels, and thermal energy storage (TES).[8,9] Among these, TES is considered to be one of the most cost-effective approaches to overcoming the intermittency of concentrated solar power.[10,11] In addition, TES can directly utilize the widely available heat resources from industrial processes such as steel mills, glass furnaces, and thermal power plants.[12,13] By 2022, TES has the second-highest installed capacity of 234 GWh and is expected to reach 800 GWh by 2030.[14]

TES technology can be further categorized into three different types, i.e., sensible thermal energy storage (STES), latent thermal energy storage (LTES), and thermochemical energy storage (TCES). At present, the only commercially available TES technology is molten salt-based STES.[15] However, the solidification issue at low temperatures and the instability at high temperatures are the main barriers to the molten salt-based STES.[16] The operating temperature window for molten salt-based STES is typically limited to 200–600 °C, leading to a small energy density of 36–180 kJ kg^{-1}.[17–19] LTES technology relies on the heat uptake and release of phase change materials (PCMs), which can achieve a two to three times larger energy density within a narrower temperature window.[20] To date, medium (100–300 °C)/high (>300 °C) temperature LTES has yet to be implemented due to various technical challenges such as the high-capital cost, poor thermal conductivity, and equipment corrosion by the liquid PCMs.[21–23]

Over the past decade, TCES, which stores thermal heat via reversible chemical reactions, has become an important research direction owing to its promise in wide operating temperature ranges and high energy storage density.[24,25] Moreover, since the energy is stored in a chemical form, TCES is capable of long-term, long-distance, and even seasonal energy

R. Cai, H. Bektas, X. Wang, K. McClintock, L. Teague, K. Yang, F. Li
Department of Chemical and Biomolecular Engineering
North Carolina State University
911 Partners Way, Raleigh, NC 27695-7905, USA
E-mail: fli5@ncsu.edu
X. Wang
Department of Chemical and Biological Engineering
Northwestern University
Evanston, IL 60208, USA
The ORCID identification number(s) for the author(s) of this article can be found under https://doi.org/10.1002/aenm.202203833.

© 2023 The Authors. Advanced Energy Materials published by Wiley-VCH GmbH. This is an open access article under the terms of the Creative Commons Attribution License, which permits use, distribution and reproduction in any medium, provided the original work is properly cited.

DOI: 10.1002/aenm.202203833

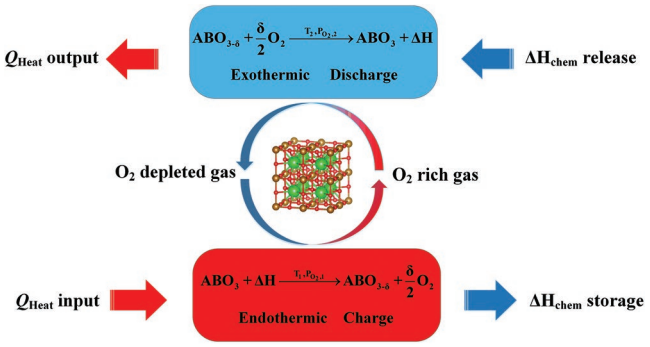

Figure 1. The typical operating scheme of perovskite-based TCES.

storage, which is difficult for STES and LTES.[26,27] Various materials have been proposed for TCES.[19,28] Among them, redox-active metal oxides have shown the greatest promise due to their ability to operate at high temperatures and without gas storage.[29,30] Recent modeling studies indicated that up to 55% round trip efficiency can be achieved with air as the only reactant.[31,32] In terms of TCES materials, perovskite oxides have been frequently investigated owing to their unique compositional/structural flexibility, high activity, and cyclic stability.[29,33,34] **Figure 1** illustrates the typical operating scheme of perovskite-based TCES materials.

Many perovskites have been reported for high-temperature TCES (**Table 1**). They generally belong to the doped $CaMnO_3$-family, the La-family, or the Sr-family. Doped $CaMnO_3$-based perovskites are the most investigated high-temperature TCES materials. Although undoped $CaMnO_{3-\delta}$ is unstable under an oxygen-lean environment at high temperatures,[35–39] doping of A-site and B-site cations has shown to improve both the stability and thermodynamic properties.[39–47] The maximum energy density reported to date was 571 kJ kg_{ABO3}^{-1} from $CaMn_{0.95}Co_{0.05}O_{3-\delta}$ under a redox cycle between 500 °C/0.2 atm O_2 and 1000 °C/10^{-5} atm O_2.[45] La-based perovskites exhibit high reaction enthalpies but require high operating temperatures (>1000 °C) without doping.[48,49] Cobalt-doping of $La_xSr_{1-x}FeO_{3-\delta}$ and $La_xSr_{1-x}MnO_{3-\delta}$ can effectively lower the operating temperatures and enhance the activity.[50–52] $La_{0.3}Sr_{0.7}Co_{0.9}Mn_{0.1}O_{3-\delta}$ demonstrated the largest chemical energy density of 250 kJ kg_{ABO3}^{-1} among the La-family perovskites under a redox cycle between 200 °C/0.9 atmO_2 and 1000 °C/0.001 atmO_2. $SrFeO_3$-based perovskites present another promising option for "low-temperature" (400–650 °C) operations.[34,53–55] The energy density of undoped $SrFeO_{3-\delta}$ was 81.7 kJ kg_{ABO3}^{-1} under a redox cycle between 400 °C/0.2 atm O_2 and 1000 °C/Ar.[56,57] The effects of various dopants on the energy storage performance of $SrFeO_3$ have also been investigated. For instance, Mn doping can significantly improve the redox enthalpy and cyclic stability of $SrFeO_3$,[55,57] while Cu substitution contributes to increasing the redox capacity of $SrFeO_{3-\delta}$.[58] $Sr_xBa_{1-x}Fe_yCo_{1-y}O_{3-\delta}$ perovskites were also investigated for TES applications. $Ba_{0.5}Sr_{0.5}CoO_{3-\delta}$ demonstrated an energy density of 202 kJ kg_{ABO3}^{-1} under a 400–1050 °C temperature swing under 0.21 atm O_2.[59]

Oxygen capacity, reaction enthalpy, and temperature and pressure operating ranges are the most critical criteria for selecting TCES materials. The structural and compositional flexibility of perovskite oxides and their complex yet tunable redox properties offer unique opportunities for TCES optimization. Perovskites with different compositions have the potential to integrate with various heat sources for a wide range of applications. However, previous research mainly relied on an empirical-based approach, which tends to be time consuming or costly. There is an urgent need for efficient screening and optimization of perovskite oxides for TCES applications.

The first principal density function theory (DFT) has shown promise in predicting the redox properties of perovskite candidates for TCES.[62,63] Previous studies showed that oxygen capacity is closely related to the oxygen vacancy formation energy (E_v).[55,64–67] Computationally predicting the reaction enthalpy of perovskite oxides has also been attempted.[43,68,69] Most of these studies started from a defect-free structure and directly calculated the reduction enthalpy from perfect perovskite phases to brownmillerite phases. However, oxygen defects often exist in perovskite oxides, even in their oxidized form.[50] High-temperature TCES operations may also exceed the order–disorder transition temperature and the brownmillerite phase may not form.[70] Therefore, oxygen vacancy concentration and structure as a function of oxygen vacancy levels need to be carefully considered. A number of high-throughput computational studies on perovskites have indicated that this approach can be a useful and promising tool in guiding the screening and optimization of perovskite oxides for chemical looping applications.[69,71,72] However, no previous research has systematically computed and optimized the perovskite materials for TCES to our best knowledge. Relevant experimental data are also limited. Therefore, it would be worthwhile to explore the effectiveness of the high-throughput approach for TCES applications.

Using high-throughput DFT calculations, this study demonstrated an accelerated approach to developing perovskite oxides for TCES. Over 2000 A/B-site doped $SrFeO_{3-\delta}$ were computed to identify promising TCES materials with satisfactory oxygen capacity and reaction enthalpy. Experimentally, 61 materials were synthesized, 45 samples with pure perovskite phases were tested for oxygen capacities, and 20 promising candidates were chosen for measuring the standard oxidation enthalpy. A chemical energy storage density of up to 157 kJ kg_{ABO3}^{-1} (≈766 kJ kg_{ABO3}^{-1} in total) was achieved by a moderate pressure swing (400 °C/0.2 atm O_2 and 1100 °C/0.01 atm O_2). These experimental and simulation data were used to develop effective optimization criteria, which are shown to be highly satisfactory in predicting the standard oxidation enthalpy (within 25.4% deviation) and oxygen capacity (a correlation coefficient of −0.64). Besides accelerating the optimization of TCES materials, the methods developed in this study can be applied in related fields such as chemical looping and catalysis.

2. Results and Discussion

2.1. High-Throughput Calculations and Material Screening

Standard reaction enthalpy and redox oxygen capacity are critical for TCES systems since their product determines the TCES density. Redox oxygen capacity is closely related to the

© 2023 The Authors. Advanced Energy Materials published by Wiley-VCH GmbH

16146840, 2023, 18, Downloaded from https://advanced.onlinelibrary.wiley.com/doi/10.1002/aenm.202203833, Wiley Online Library on [17/03/2025]. See the Terms and Conditions (https://onlinelibrary.wiley.com/terms-and-conditions) on Wiley Online Library for rules of use; OA articles are governed by the applicable Creative Commons License

Table 1. A summary of key parameters of perovskite oxides for the thermochemical energy storage.

TES materials	T[a)]	P_{O2}[b)]	$\Delta\delta$[c)]	$\Delta H_O(\delta)$[d)]	$.\Delta H_{chem}$[e)]
$CaMnO_{3-\delta}$[60]	200–1100	0.18–0.008	0.22	170–216	273
$CaTi_{0.2}Mn_{0.8}O_{3-\delta}$[40]	200–1250	0.9–0.001	0.29	190–210	390
$CaAl_{0.2}Mn_{0.8}O_{3-\delta}$[40]	200–1250	0.9–0.001	0.32	120–195	370
$CaFe_{0.1}Mn_{0.9}O_{3-\delta}$[60]	200–1200	0.18–0.008	0.27	114–214	344
$CaFe_{0.3}Mn_{0.7}O_{3-\delta}$[60]	200–1200	0.18–0.008	0.23	64–164	222
$CaCr_{0.05}Mn_{0.95}O_{3-\delta}$[41]	500–1000	0.17–0.0001	0.23	150–208	392
$Ca_{0.95}Sr_{0.05}MnO_{3-\delta}$[42]	500–1000	0.17–0.0001	0.30	184–260	555
$Ca_{0.9}Sr_{0.1}MnO_{3-\delta}$[41,42]	500–1000	0.17–0.0001	0.28	168–240	455
$Ca_{0.75}Sr_{0.25}MnO_{3-\delta}$[43]	500–1000	0.21–0.0001	0.34	173–187	398
$Ca_{0.6}Sr_{0.4}MnO_{3-\delta}$[44]	500–1000	0.21–0.00001	0.32	123–148	300
$CaCo_{0.05}Mn_{0.95}O_{3-\delta}$[45]	500–1000	0.21–0.00001	0.36	170–380	571
$CaCo_{0.1}Mn_{0.9}O_{3-\delta}$[45]	500–1000	0.21–0.00001	0.33	160–250	424
$Ca_{0.9}La_{0.1}MnO_{3-\delta}$[46]	500–1200	0.18–0.008	0.17	190–227	265
$CaCu_{0.2}Mn_{0.8}O_{3-\delta}$[47]	500–1000	0.21–0.00001	–	–	430
$CaMg_{0.1}Mn_{0.9}O_{3-\delta}$[47]	500–1000	0.21–0.00001	–	–	280
$La_{0.1}Sr_{0.9}Co_{0.9}Mn_{0.1}O_{3-\delta}$[50]	200–1250	0.9–0.001	0.43	18–187	220
$La_{0.3}Sr_{0.7}Co_{0.9}Mn_{0.1}O_{3-\delta}$[50]	200–1250	0.9–0.001	0.46	40–186	250
$La_{0.3}Sr_{0.7}Co_{0.8}Mn_{0.2}O_{3-\delta}$[50]	200–1250	0.9–0.001	0.41	67–174	230
$La_{0.2}Sr_{0.8}Fe_{0.2}Co_{0.8}O_{3-\delta}$[50]	200–1250	0.9–0.001	0.49	3–233	210
$La_{0.3}Sr_{0.7}Fe_{0.1}Co_{0.9}O_{3-\delta}$[50]	200–1250	0.9–0.001	0.46	15–210	220
$La_{0.3}Sr_{0.7}Fe_{0.3}Co_{0.7}O_{3-\delta}$[50]	200–1250	0.9–0.001	0.45	15–220	220
$SrFeO_{3-\delta}$[56]	400–1000	0.21–0.0001[f)]	0.28	–	80
$SrCoO_{3-\delta}$[56]	400–1000	0.21–0.0001[f)]	0.27	–	48
$SrMnO_{3-\delta}$[56]	400–1000	0.21–0.0001[f)]	0.05	–	34
$Sr_{0.3}Ba_{0.7}CoO_{3-\delta}$[52]	500–1150	0.21 (isobaric)	0.29	–	172
$Sr_{0.5}Ba_{0.5}CoO_{3-\delta}$[52]	500–1150	0.21	0.21	–	78
$Sr_{0.7}Ba_{0.3}CoO_{3-\delta}$[52]	500–1150	0.21	0.21	–	186
$SrFeO_{3-\delta}$[61]	600–950	0.2–0.000001[f)]	0.16	–	53
$SrFe_{0.2}Co_{0.8}O_{3-\delta}$[61]	600–950	0.2–0.000001[f)]	0.14	–	45
$Sr_{0.5}Ba_{0.5}Fe_{0.2}Co_{0.8}O_{3-\delta}$[61]	600–950	0.2–0.000001[f)]	0.11	–	47
$BaCoO_{3-\delta}$[61]	600–950	0.2–0.000001[f)]	0.49	–	292
$Sr_{0.5}Ba_{0.5}CoO_{3-\delta}$[61]	600–950	0.2–0.000001[f)]	0.26	–	173
$Sr_{0.5}Ba_{0.5}CoO_{3-\delta}$[59]	400–1050	0.21	0.31	–	202

[a)] T: range of the operating temperatures, °C; [b)] P_{O2}: range of the operating partial pressures of oxygen, atm; [c)] $\Delta\delta$: oxygen nonstoichiometry change; [d)] $\Delta H_O(\delta)$: reaction enthalpy at different δs, kJ mol^{-1} O. Some data were extracted from the figures in the literature. Reaction enthalpy data are not available in the papers using the DSC method to obtain the energy density; [e)] ΔH_{chem}: thermochemical energy storage density, kJ kg^{-1} ABO_3; [f)] The sample was reduced at high temperatures in Ar and then reoxidized in the air.

operating temperature. As such, multiple criteria are required for choosing a suitable candidate for TCES. At a specific temperature, ΔG needs to be within a suitable range to facilitate oxygen release and uptake. Since a small ΔG and a large ΔH are desirable for TCES, they were both used as the descriptors when analyzing the results from the high-throughput DFT calculations of the 2003 $Sr_xA_{1-x}Fe_yB_{1-y}O_{3-\delta}$ candidates.

We began with $SrFeO_{3-\delta}$ as the parent structure and introduced various dopants to the A- and/or B-sites ($Sr_xA_{1-x}Fe_yB_{1-y}O_{3-\delta}$). Based on their tolerance factors,[73,74] we screened out potentially unstable compositions. For the remaining 2003 perovskite compositions which are likely to be structurally stable, we conducted DFT calculations to obtain their ΔH and ΔG at different nonstoichiometry (δ) levels. Meanwhile, thermodynamic criteria (ΔG) for materials selection were determined based on the operational requirements. Using these criteria and computational results, promising TCES candidates were selected for the quick experimental screening of oxygen capacities. The materials with high (calculated) ΔH and suitable oxygen capacities were subjected to the ΔH measurements, finally generating the optimized TCES materials.

The selection of TCES materials is also dependent upon the operating temperature range. A 400–800 °C temperature range, which is readily compatible with thermal power plants

© 2023 The Authors. Advanced Energy Materials published by Wiley-VCH GmbH

16146840, 2023, 18, Downloaded from https://advanced.onlinelibrary.wiley.com/doi/10.1002/aenm.202203833, Wiley Online Library on [17/03/2025]. See the Terms and Conditions (https://onlinelibrary.wiley.com/terms-and-conditions) on Wiley Online Library for rules of use; OA articles are governed by the applicable Creative Commons License

and many industrial processes, was chosen in this study. At the upper (800 °C) and the lower (400 °C) limits, the suitable range of ΔG for triggering the oxygen release can be directly calculated from Equation (1) .

$$\Delta G = -\frac{1}{2} RT \ln \frac{P_{O_2}}{P^0} \tag{1}$$

Most studies on TCES materials exposed the samples to very low oxygen concentrations (e.g., ≤10–^{4} atm) during the energy storage step. Although this would increase the nominal energy storage capacity, the need to create very low oxygen partial pressure environments, whether through vacuuming or large steam dilution, would lead to low round-trip efficiencies and high costs. Therefore, it is preferable to use relatively high oxygen partial pressures from a practical standpoint.[32,75,76] This study adopts a pressure swing between P_{O2} = 0.01 atm (energy storage) and P_{O2} = 0.2 atm (energy release). This corresponds to ΔG ranges of 0.047–0.134 eV at 400 °C and 0.074–0.213 eV at 800 °C. Considering the error range of the DFT calculations (–0.3 to 0.5 eV) identified by our previous study,[74] the criteria for screening potentially suitable materials were relaxed to $\Delta G_{\mathrm{DFT}} \begin{cases} \in [-0.253, 0.634]\,\mathrm{eV\ at\ 400°C} \\ \in [-0.226, 0.713]\,\mathrm{eV\ at\ 800°C} \end{cases}$. Past experience indicated that oxygen nonstoichiometry (δ) in TCES materials is usually less than 0.3 under a moderate oxygen partial pressure of >0.001 atm. Therefore, our initial screening focused on a δ range of 0–0.25, i.e., the average between $\Delta G_{0\text{–}0.125}$ and $\Delta G_{0.125\text{–}0.25}$ calculated from DFT was compared to the aforementioned criteria.

775 samples are potentially suitable based on these criteria (Figure S1, Supporting Information). Most samples containing Ti, Sm, La, and Cu were removed from consideration due to undesirable ΔG. Ti, Sm, and La dopants tended to increase the temperatures for oxygen release, leading to an excessively large ΔG. In contrast, the Cu dopant had the opposite impact on ΔG.

With respect to the other descriptor, i.e., ΔH, **Figure 2**a summarizes its probability distribution for the 775 candidates resulting from ΔG screening. It is clearly seen that ΔH can be tuned, through cation doping, over a large range of –0.3–3.3 eV.

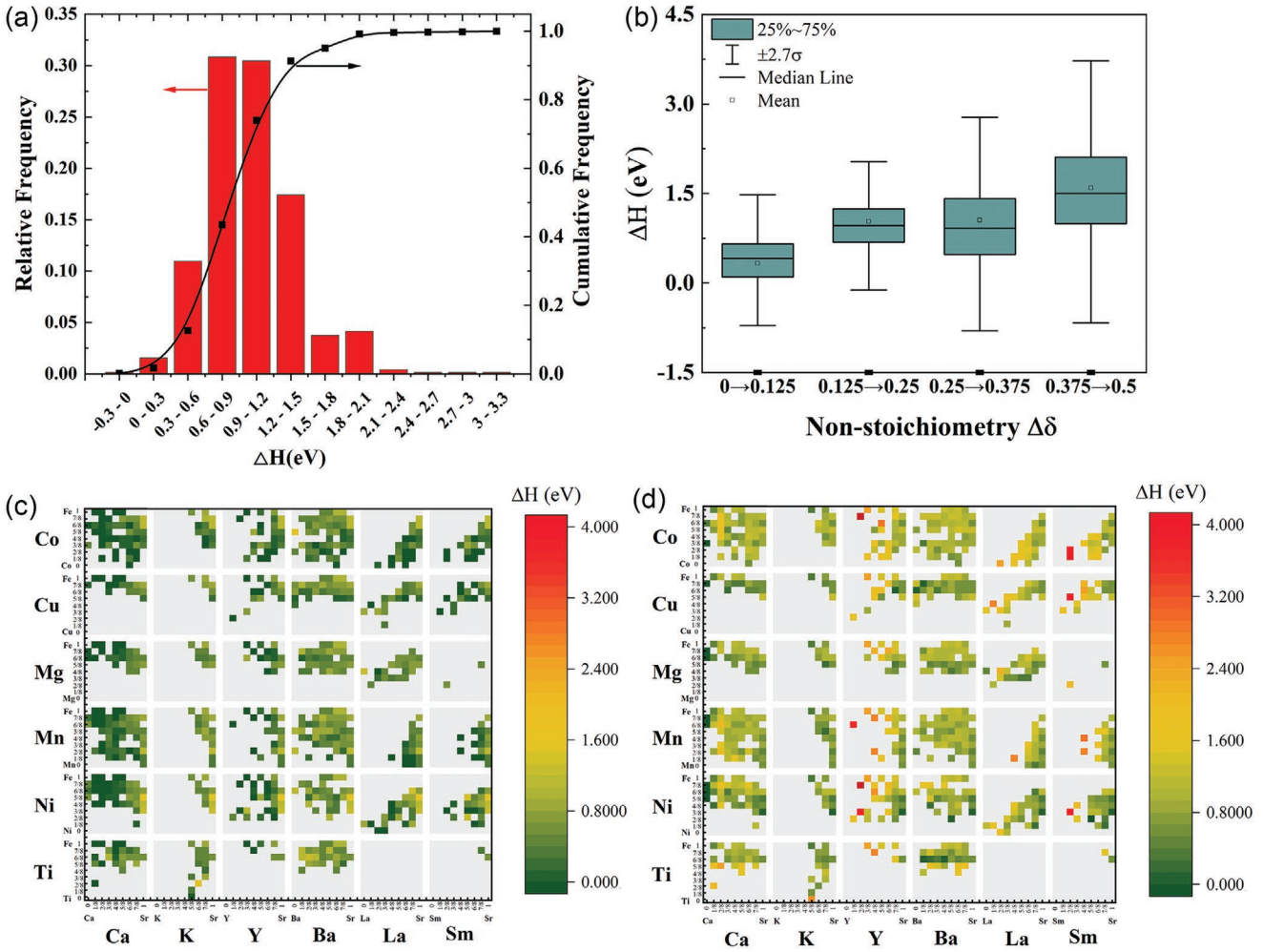

Figure 2. High-throughput calculation results of the reaction enthalpy at 400 °C. a) Probability distribution of ΔH for the screened candidates. b) A statistic summary of ΔH for the screened candidates within different δ ranges. c) A heatmap of the screened candidates within the δ range of 0–0.125. d) A heatmap of the screened candidates within the δ range of 0.125–0.25.

© 2023 The Authors. Advanced Energy Materials published by Wiley-VCH GmbH

16146840, 2023, 18, Downloaded from https://advanced.onlinelibrary.wiley.com/doi/10.1002/aenm.202203833, Wiley Online Library on [17/03/2025]. See the Terms and Conditions (https://onlinelibrary.wiley.com/terms-and-conditions) on Wiley Online Library for rules of use; OA articles are governed by the applicable Creative Commons License

80% of the materials fell within the range of 0.3–1.5 eV, i.e., 29–145 kJ mol^{-1} O. The statistical summary of ΔH at different δ ranges is shown in Figure 2b. In general, ΔH increased with the oxygen vacancy level. This is consistent with most literature reports on perovskites with cubic structures.[50,57,60,77–79] The wide range of ΔH values at different δs also indicates the necessity for covering multiple δ levels. In addition, since a considerable number of the perovskite materials for TCES either do not start from a perfect stoichiometry (i.e., $\delta > 0$ under an oxidized state) or do not release too much lattice oxygen (i.e., $\delta < 0.5$ under a reduced state), directly calculating the reduction enthalpy from perfect perovskite phases to brownmillerite phases may lead to mispredictions. The simulation results also revealed a less significant correlation between ΔH and temperature, which has also been reported in previous studies.[80] The ΔH heatmaps of the screened perovskite candidates are shown in Figure 2c,d and Figure S2 in the Supporting Information.

Besides ΔG and ΔH, the cost of the material is also important. Therefore, materials doped with costly elements, i.e., Ni, Co, Cu, Sm, and Y, were excluded from experimental investigations. K-doped materials were also excluded due to potential corrosion issues. The ultimate screening list is summarized in Table S1 in the Supporting Information. 209 candidates were sorted by $\Delta H(\delta = 0–0.25)$ normalized by molecular weight, 61 materials were synthesized, and 45 samples with negligible phase impurities were tested for their redox oxygen capacity. Figure S8 in the Supporting Information summarizes the X-ray Diffraction (XRD) spectra of all 61 materials prepared.

2.2. Redox Oxygen Capacity and Energy Density Performance

The oxygen capacities under different conditions are summarized in **Table 2**, with all the underlying data reported in Table S2 in the Supporting Information. Under the redox condition of 400 °C/0.2 atm O_2 and 800 °C/0.01 atm O_2, the highest oxygen capacity was 2.11 wt% for $Sr_{0.75}Ba_{0.25}Fe_{0.875}Mg_{0.125}O_{3-\delta}$, while $Sr_{0.5}La_{0.5}Fe_{0.125}Mn_{0.875}O_{3-\delta}$ showed negligible oxygen release. The thermogravimetric analyzer (TGA) profile of $Sr_{0.75}Ba_{0.25}Fe_{0.875}Mg_{0.125}O_{3-\delta}$ is presented in Figure S3 in the Supporting Information. Ba-doped or Ba/Mg-codoped $SrFeO_{3-\delta}$ exhibited considerable oxygen capacities at low temperatures and high oxygen partial pressures. Compared to $SrFeO_{3-\delta}$, $Sr_{0.75}Ba_{0.25}Fe_{0.875}Mg_{0.125}O_{3-\delta}$ and $Sr_{0.875}Ba_{0.125}FeO_{3-\delta}$ favored oxygen release at higher oxygen pressures (Figure S4, Supporting Information). The oxygen absorption/desorption kinetics also increased with the Ba dopant, which would benefit the power density (Figure S5, Supporting Information). However, when Ba doping was larger than 0.375 (e.g., $Sr_{0.5}Ba_{0.5}FeO_{3-\delta}$), phase segregation of $BaFeO_3$ and $SrFeO_3$ was observed through XRD. Interestingly, phase segregation at high Ba levels can be inhibited by substituting Fe with small amounts of Mg and Ti in the B-site, e.g., $Sr_{0.25}Ba_{0.75}Fe_{0.875}Mg_{0.125}O_{3-\delta}$ and $Sr_{0.125}Ba_{0.875}Fe_{0.875}Ti_{0.125}O_{3-\delta}$. Even though the oxygen capacities were slightly lower, they all demonstrated sufficient oxygen capacity under an isothermal condition at 400 °C even though 0.01 atm O_2 was used as the lower bound for oxygen partial pressure, which was three orders of magnitude higher than typical testing conditions. In general, Ba-based perovskites exhibited superior performance in O_2 redox capacity within the 400–800 °C range, which is highly compatible with steam-based power plants.

$Sr_xCa_{1-x}Fe_yMn_{1-y}O_{3-\delta}$ perovskites were another group of materials showing promising TCES performance. They exhibited the highest changes in δ owing to their smaller molar masses. Mn-doping tended to increase the temperature window for oxygen release. A considerable amount of oxygen was released in the range of 800–1100 °C. $Sr_{0.125}Ca_{0.875}Fe_{0.25}Mn_{0.75}O_{3-\delta}$, $Sr_{0.25}Ca_{0.75}Fe_{0.375}Mn_{0.625}O_{3-\delta}$, and $Sr_{0.375}Ca_{0.625}Fe_{0.125}Mn_{0.875}O_{3-\delta}$ all exhibited oxygen releases >2.8 wt% under the redox condition between 400 °C/0.2 atm O_2 and 1100 °C/Ar. In particular, $Sr_{0.375}Ca_{0.625}Fe_{0.125}Mn_{0.875}O_{3-\delta}$ and $Sr_{0.125}Ca_{0.875}Fe_{0.25}Mn_{0.75}O_{3-\delta}$ had an oxygen capacity >2.1 wt% even with a redox condition between 400 °C/0.2 atm O_2 and 1100 °C/0.01 atm O_2. This moderate oxygen atmosphere is helpful for the flexible operation of industrial TCES applications.

Based on the oxygen capacity under the redox condition between 400 °C/0.2 atmO_2 and 1100 °C/Ar, 20 materials with oxygen releases >1 wt% were selected to measure their reaction enthalpies. **Figure 3** summarizes the key results for a few selected materials, with all the underlying thermodynamic data reported in Figures S6 and S7 in the Supporting Information. ΔH of the tested materials varied from 20 to 160 kJ mol^{-1} O, while δ covered nearly the whole range of 0–0.5. In general, ΔH increased with the oxygen vacancy, which is consistent with most reported data of $SrFeO_3$-based perovskites.[57] It is clear that the dopant types and concentrations significantly changed ΔH, but some general trends can be captured from the tested materials. As mentioned above, Ba doping tended to decrease the temperatures for oxygen release, but the corresponding ΔH was also lower compared to La-doped, Ca-doped, or undoped samples. The ΔH of the Ba-doped $SrFeO_{3-\delta}$ samples slightly decreased with the increase in the Ba dopant. This is consistent with Bush et al.'s study on $Sr_{1-x}Ba_xFeO_{3-\delta}$ for air separation.[77,81] Mg-doping stabilized the $Sr_xBa_{1-x}FeO_{3-\delta}$ at high-Ba doping conditions and facilitated the oxygen release but negatively affected the ΔH.

The effects of Mn-dopants varied with A-site dopant types. For the Sr-Ca perovskites, Mn doping increased the oxygen release temperature but concurrently led to a higher ΔH. For instance, for the $Sr_{0.25}Ca_{0.75}Fe_yMn_{1-y}O_{3-\delta}$ materials and the $Sr_{0.375}Ca_{0.625}Fe_yMn_{1-y}O_{3-\delta}$ materials, ΔH significantly increased with the increase in the substitution of Mn in the B-site. However, a small quantity of Mn-doping in $Sr_{0.75}Ba_{0.25}FeO_{3-\delta}$ significantly affected ΔH and the oxygen release performance. Among all the tested materials, $Sr_{0.125}Ca_{0.875}Fe_{0.25}Mn_{0.75}O_{3-\delta}$ displayed the highest ΔH of 160 kJ mol^{-1} O with $\Delta\delta$ of 0.3 under a redox condition between 400 °C/0.2 atmO_2 and 1100 °C/Ar.

The chemical energy storage densities (ΔH_{chem}) of the screened materials are summarized in **Figure 4**, with the details summarized in Table S3 in the Supporting Information. Air can easily trigger the redox reaction of Ba-doped samples. A higher temperature or a lower oxygen partial pressure only leads to a minor increase in ΔH_{chem}, especially for $Sr_{0.25}Ba_{0.75}Fe_{0.875}Mg_{0.125}O_{3-\delta}$. $Sr_{0.875}Ba_{0.125}FeO_{3-\delta}$ exhibited the largest ΔH_{chem} of 83 kJ kg_{ABO3}^{-1} under an isobaric air condition between 400 and 800 °C. The ability to operate isobarically in the air instead of under large oxygen partial pressure swings would greatly simplify the

© 2023 The Authors. Advanced Energy Materials published by Wiley-VCH GmbH

16146840, 2023, 18, Downloaded from https://advanced.onlinelibrary.wiley.com/doi/10.1002/aenm.202203833, Wiley Online Library on [17/03/2025]. See the Terms and Conditions (https://onlinelibrary.wiley.com/terms-and-conditions) on Wiley Online Library for rules of use; OA articles are governed by the applicable Creative Commons License

Table 2. Experimental oxygen capacities of the DFT predicted materials at different redox conditions.

Parameters [wt%]	Isothermal condition				Pressure + temperature swing		
	400 °C		800 °C		400–800 °C		
Material	0.2–0.01 atm O_2	0.2 atm O_2-Ar	0.2–0.01 atm O_2	0.2 atm O_2-Ar	0.2 atm O_2	0.2–0.01 atm O_2	0.2 atm O_2-Ar
$SrFeO_{3-\delta}$	0.26	0.54	0.51	0.97	1.50	2.01	2.46
$Sr_{0.75}Ba_{0.25}Fe_{0.875}Mg_{0.125}O_{3-\delta}$	0.65	1.02	0.71	1.02	1.39	2.11	2.41
$SrFe_{0.875}Mn_{0.125}O_{3-\delta}$	0.36	0.82	0.58	1.14	1.22	1.80	2.37
$Sr_{0.875}Ba_{0.125}FeO_{3-\delta}$	0.24	0.61	0.45	0.85	1.51	1.96	2.36
$Sr_{0.75}Ba_{0.25}FeO_{3-\delta}$	0.30	0.74	0.42	0.78	1.43	1.85	2.21
$Sr_{0.625}Ba_{0.375}FeO_{3-\delta}$	0.30	0.81	0.34	0.60	1.42	1.76	2.03
$Sr_{0.625}Ba_{0.375}Fe_{0.875}Mg_{0.125}O_{3-\delta}$	0.44	0.99	0.42	0.69	1.33	1.75	2.02
$Sr_{0.875}Ba_{0.125}Fe_{0.875}Mn_{0.125}O_{3-\delta}$	0.28	0.60	0.44	0.81	1.19	1.64	2.00
$Sr_{0.875}Ca_{0.125}Fe_{0.875}Mn_{0.125}O_{3-\delta}$	0.31	0.64	0.41	0.79	1.22	1.63	2.01
$Sr_{0.25}Ba_{0.75}Fe_{0.875}Mg_{0.125}O_{3-\delta}$	0.72	1.27	0.44	0.69	1.14	1.58	1.83
$SrFe_{0.75}Ti_{0.25}O_{3-\delta}$	0.17	0.48	0.35	0.72	1.07	1.42	1.79
$Sr_{0.125}Ba_{0.875}Fe_{0.875}Ti_{0.125}O_{3-\delta}$	0.49	0.81	0.25	0.53	1.07	1.33	1.61
$Sr_{0.625}Ba_{0.375}Fe_{0.875}Mn_{0.125}O_{3-\delta}$	0.14	0.76	0.30	0.59	1.02	1.32	1.61
$Sr_{0.75}Ba_{0.25}Fe_{0.875}Mn_{0.125}O_{3-\delta}$	0.08	0.65	0.31	0.63	0.95	1.27	1.59
$Sr_{0.875}Ba_{0.125}Fe_{0.625}Ti_{0.375}O_{3-\delta}$	0.19	0.45	0.22	0.42	0.89	1.20	1.56
$Sr_{0.75}Ca_{0.25}Fe_{0.75}Ti_{0.25}O_{3-\delta}$	0.21	0.68	0.29	0.56	0.89	1.18	1.44
$Sr_{0.75}Ca_{0.25}Fe_{0.75}Mn_{0.25}O_{3-\delta}$	0.23	0.58	0.25	0.58	0.93	1.18	1.51
$Sr_{0.25}Ba_{0.75}Fe_{0.875}Ti_{0.125}O_{3-\delta}$	0.30	0.75	0.15	0.28	0.97	1.12	1.25
$Sr_{0.875}Ca_{0.125}Fe_{0.625}Ti_{0.375}O_{3-\delta}$	0.28	0.55	0.39	0.63	0.72	1.11	1.35
$Sr_{0.75}Ca_{0.25}Fe_{0.625}Mn_{0.375}O_{3-\delta}$	0.21	0.51	0.27	0.67	0.75	1.01	1.42
$Sr_{0.75}La_{0.25}Fe_{0.375}Mn_{0.625}O_{3-\delta}$	0.08	0.31	0.33	0.79	0.59	0.91	1.37
$Sr_{0.875}La_{0.125}Fe_{0.75}Mn_{0.25}O_{3-\delta}$	0.10	0.33	0.29	0.66	0.61	0.91	1.27
$Sr_{0.875}Ca_{0.125}Fe_{0.875}Mg_{0.125}O_{3-\delta}$	0.01	0.72	0.37	0.67	0.49	0.86	1.16
$Sr_{0.875}La_{0.125}Fe_{0.625}Mn_{0.375}O_{3-\delta}$	0.19	0.38	0.30	0.67	0.54	0.84	1.21
$Sr_{0.125}Ca_{0.875}Fe_{0.25}Mn_{0.75}O_{3-\delta}$	0.10	0.26	0.31	1.00	0.48	0.80	1.49
$Sr_{0.75}La_{0.25}Fe_{0.75}Mg_{0.25}O_{3-\delta}$	0.50	0.54	0.12	0.27	0.67	0.79	0.94
$Sr_{0.25}Ca_{0.75}Fe_{0.25}Mn_{0.75}O_{3-\delta}$	0.09	1.50	0.30	1.03	0.48	0.78	1.50
$Sr_{0.75}Ba_{0.25}Fe_{0.625}Ti_{0.375}O_{3-\delta}$	0.04	0.38	0.17	0.34	0.60	0.77	0.94
$Sr_{0.75}Ba_{0.25}Fe_{0.5}Ti_{0.5}O_{3-\delta}$	0.17	0.34	0.18	0.35	0.56	0.74	0.91
$Sr_{0.25}Ca_{0.75}Fe_{0.375}Mn_{0.625}O_{3-\delta}$	0.06	0.25	0.26	0.90	0.44	0.69	1.34
$Sr_{0.625}Ca_{0.375}Fe_{0.625}Ti_{0.375}O_{3-\delta}$	0.04	0.28	0.14	0.32	0.55	0.69	0.87
$Sr_{0.375}Ca_{0.625}Fe_{0.125}Mn_{0.875}O_{3-\delta}$	0.00	0.16	0.28	1.12	0.36	0.64	1.48
$Sr_{0.375}Ca_{0.625}Fe_{0.5}Mn_{0.5}O_{3-\delta}$	0.03	0.25	0.18	0.70	0.44	0.62	1.14
$Sr_{0.625}Ca_{0.375}Fe_{0.5}Ti_{0.5}O_{3-\delta}$	0.02	0.27	0.10	0.24	0.36	0.54	0.68
$Sr_{0.25}Ca_{0.75}Fe_{0.625}Ti_{0.375}O_{3-\delta}$	0.20	0.66	0.28	0.69	0.07	0.35	0.76
$Sr_{0.5}Ca_{0.5}Fe_{0.625}Ti_{0.375}O_{3-\delta}$	0.03	0.15	0.07	0.20	0.27	0.34	0.47
$Sr_{0.25}Ca_{0.75}Fe_{0.625}Mn_{0.375}O_{3-\delta}$	0.04	0.20	0.12	0.47	0.22	0.33	0.69
$BaFe_{0.625}Mn_{0.375}O_{3-\delta}$	0.00	0.04	0.10	0.07	0.29	0.33	0.42
$Sr_{0.375}Ca_{0.625}Fe_{0.75}Ti_{0.25}O_{3-\delta}$	0.00	0.14	0.04	0.15	0.26	0.30	0.41
$Sr_{0.125}Ca_{0.875}Fe_{0.75}Mn_{0.25}O_{3-\delta}$	0.15	0.59	0.22	0.92	0.07	0.29	0.99
$Sr_{0.25}Ca_{0.75}Fe_{0.75}Mn_{0.25}O_{3-\delta}$	0.06	0.35	0.10	0.59	0.16	0.26	2.14
$SrFe_{0.375}Mn_{0.625}O_{3-\delta}$	0.04	0.40	0.09	0.64	0.16	0.25	0.79
$Sr_{0.125}Ca_{0.875}Fe_{0.25}Ti_{0.75}O_{3-\delta}$	0.07	0.23	0.10	0.21	0.13	0.23	0.34
$Sr_{0.125}Ca_{0.875}Fe_{0.625}Ti_{0.375}O_{3-\delta}$	0.03	0.13	0.05	0.13	0.06	0.11	0.19
$Sr_{0.5}La_{0.5}Fe_{0.125}Mn_{0.875}O_{3-\delta}$	–0.09	–0.04	–0.03	–0.01	0.02	–0.01	0.02

 © 2023 The Authors. Advanced Energy Materials published by Wiley-VCH GmbH

16146840, 2023, 18, Downloaded from https://advanced.onlinelibrary.wiley.com/doi/10.1002/aenm.202203833, Wiley Online Library on [17/03/2025]. See the Terms and Conditions (https://onlinelibrary.wiley.com/terms-and-conditions) on Wiley Online Library for rules of use; OA articles are governed by the applicable Creative Commons License

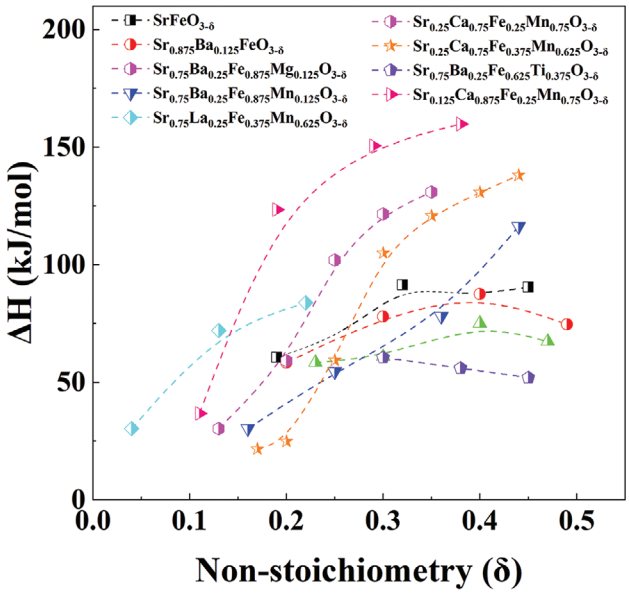

Figure 3. Reaction enthalpies of selected materials.

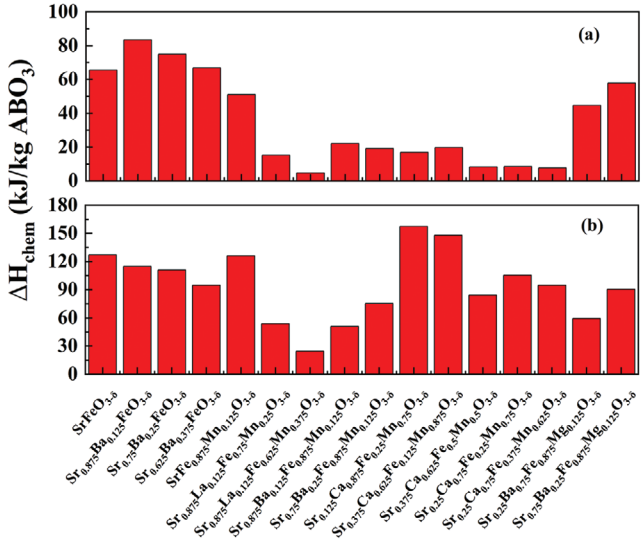

Figure 4. Chemical energy storage density of the screened materials under different redox conditions: a) 400 °C/0.2 atm O_2 and 800 °C/0.2 atm O_2 and b) 400 °C/0.2 atm O_2 and 1100 °C/0.01 atm.

system design and operations. In contrast, $Sr_xCa_{1-x}Fe_yMn_{1-y}O_{3-\delta}$ barely released O_2 and absorbed heat at low temperatures, but ΔH_{chem} was significantly improved when the temperature was above 800 °C. $Sr_{0.125}Ca_{0.875}Fe_{0.25}Mn_{0.75}O_{3-\delta}$ achieved a ΔH_{chem} of 157 kJ kg_{ABO3}^{-1} under a redox condition between 400 °C/0.2 atm O_2 and 1100 °C/0.01 atm O_2 and a ΔH_{chem} of 285 kJ kg_{ABO3}^{-1} under a redox condition between 400 °C/0.2 atm O_2 and 1100 °C/Ar. Based on an estimated heat capacity of 0.87 kJ kg^{-1} K^{-1},[41] the total energy storage capacities under the two aforementioned conditions are 766 and 894 kJ/kg_{ABO3}, respectively.

2.3. Assessment of the Model Effectiveness

As shown in **Figure 5**a, all the samples with appreciable oxygen capacities showed consistency between experimental measurement and DFT prediction in terms of ΔH, with an average standard deviation of 25.4%. 65% of the data fell within ±25%, and 90% of the data fell within ±35%. This is understandable since the ΔH and ΔG are closely related. A misprediction of ΔG will likely lead to a misprediction of ΔH. Therefore, a simple screening experiment on oxygen capacity, which would rule out most samples with mispredicted ΔG, can substantially increase the accuracy of the DFT prediction of ΔH. $Sr_{0.125}Ca_{0.875}Fe_{0.25}Mn_{0.75}O_{3-\delta}$ showed significant deviation, likely due to the simplified assumptions we adopted for the high throughput computation: DFT calculation started from a cubic $SrFeO_3$ structure without structural relaxation to maintain the computational efficiency, but $Sr_{0.125}Ca_{0.875}Fe_{0.25}Mn_{0.75}O_{3-\delta}$ was an orthorhombic structure based on XRD. Figure 5b compares the range of the computed ΔH with the measured ΔH. A range was provided since it changes with oxygen nonstoichiometry. For the measured ΔH, the range covered the maximum and minimum ΔH obtained experimentally at different δ. The range of the DFT predicted ΔH included ΔH_δ = 0–0.125 and ΔH_δ = 0.125–0.25. For most materials with sufficient oxygen capacities, the DFT predicted ΔH largely overlapped with the experimental measurements.

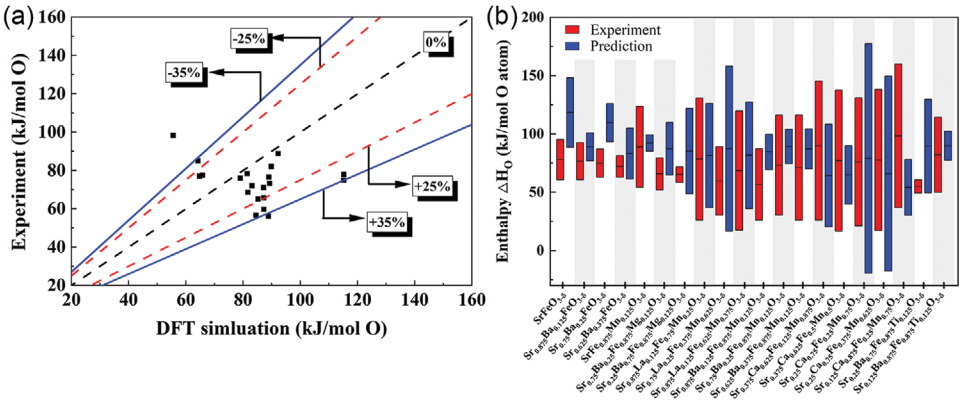

Figure 5. Comparison between experimental measurement and DFT prediction of ΔH for different perovskites: a) relative deviation of average ΔH and b) ranges of ΔH.

© 2023 The Authors. Advanced Energy Materials published by Wiley-VCH GmbH

16146840, 2023, 18, Downloaded from https://advanced.onlinelibrary.wiley.com/doi/10.1002/aenm.202203833, Wiley Online Library on [17/03/2025]. See the Terms and Conditions (https://onlinelibrary.wiley.com/terms-and-conditions) on Wiley Online Library for rules of use; OA articles are governed by the applicable Creative Commons License

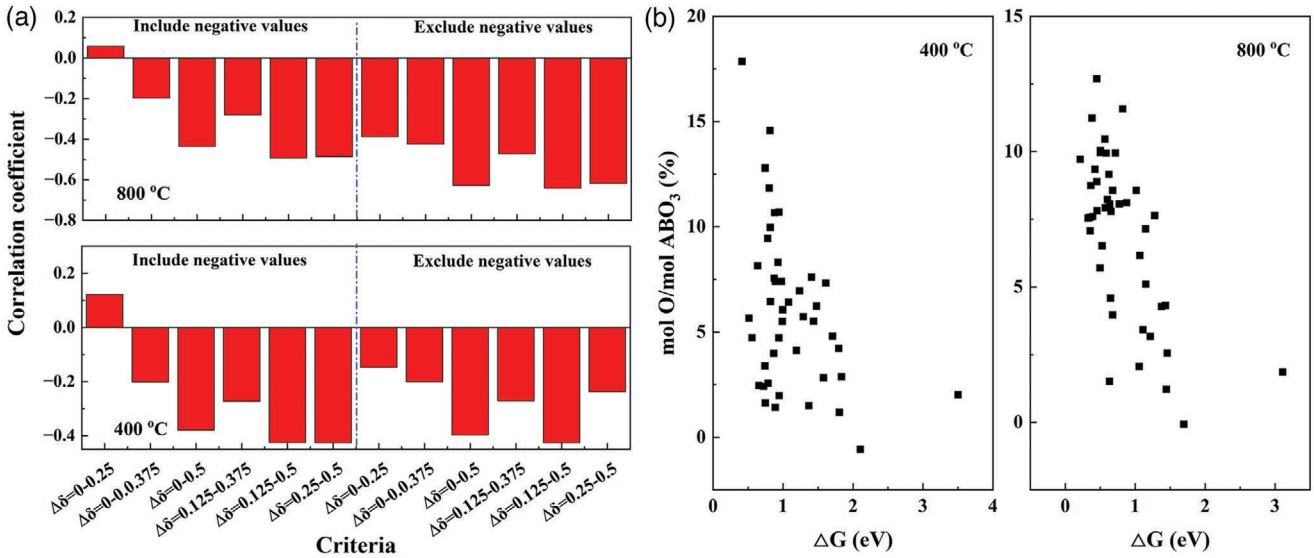

Figure 6. Comparison between experimental measurements and DFT predictions using different criteria: a) correlation factor between ΔG and oxygen capacity and b) relationship between ΔG and oxygen capacity using the non-negative ΔG within the range of 0.125–0.5.

2.4. Improved Criteria and Approaches for TCES Optimization

Although our initial screening criteria were sufficient for predicting the ΔH, they led to non-negligible deviation in predicting oxygen capacities. Based on the experimental data, we tested alternative screening criteria to improve the effectiveness in predicting the oxygen capacity of perovskite oxides. Due to the limitation of the supercell size, DFT calculations have limited resolutions for δ change. In our current calculation, the minimum δ change is 0.125. Therefore, we attempted to correlate the experimentally measured oxygen capacity with the DFT calculated ΔG at different δ variation ranges to determine the most effective descriptor for the oxygen capacity. Correlation coefficients, defined in Equation (2), were used to describe the relationship between oxygen capacity and ΔG within different δ ranges.

$$Correl(\Delta G, n_{oc}) = \frac{\sum_{i=1}^{N}(\Delta G_i - \Delta\bar{G})(n_{oc,i} - \bar{n}_{oc,i})}{\sum_{i=1}^{N}(\Delta G_i - \Delta\bar{G})^2 \sum_{i=1}^{N}(n_{oc,i} - \bar{n}_{oc,i})^2} \quad (2)$$

The correlations between the ΔG and oxygen capacity at 400 and 800 C were investigated. These two temperatures were selected since they would cover a wide range of potential heat sources and applications. A smaller but non-negative ΔG indicates the thermodynamic favorability of oxygen release from the perovskite. Therefore, oxygen capacity and ΔG should present a negative correlation. Since some DFT calculated ΔG were less than zero and were likely to be inaccurate, the correlation coefficients were also calculated by resetting the negative ΔG to 0. The oxygen capacities under the isothermal redox condition between 0.2 atm O_2 and Ar were used for the calculation.

As shown in **Figure 6**a, the selection of ΔG within different δ ranges significantly affected the correlation factor. The best prediction was obtained using the non-negative ΔG within the range of 0.125–0.5, which was also consistent with the typical operating δ range of the tested samples between 0.1 and 0.45. The correlation coefficient was around −0.64 at 800 °C, demonstrating a moderately negative correlation which would be highly useful for screening purposes. The correlation was less significant at 400 °C, which may have resulted from the kinetic limitation of some perovskite materials. The relationship between ΔG and oxygen capacity using the non-negative ΔG within the range of 0.125–0.5 is shown in Figure 5b. Based on the aforementioned discussion, a flowchart for high throughput screening of perovskite oxides for TCES is proposed in **Figure 7**. This improved screening workflow can enhance the efficiency of TCES material development by approximately one order of magnitude when compared to the conventional trial-and-error method.

3. Conclusions

The current study reports an effective high-throughput combinatorial approach for accelerated development and optimization of perovskite oxides for thermochemical energy storage. Based on DFT calculation results of more than 2000 A-site and/or B-site substituted $SrFeO_{3-\delta}$ perovskites at various oxygen nonstoichiometry (δ) levels, 61 promising TCES candidates were selected and prepared. Nearly all the samples formed perovskite phases as their main compositions. Of these, 45 samples showed negligible phase impurities and were thoroughly investigated experimentally, including detailed measurements of the redox thermodynamic parameters of 20 samples. Many of these samples showed promising TCES properties. $Sr_{0.875}Ba_{0.125}FeO_{3-\delta}$ exhibited a chemical energy storage density of 85 kJ kg_{ABO3}^{-1} under an isobaric air condition between 400 and 800 °C and $Sr_{0.125}Ca_{0.875}Fe_{0.25}Mn_{0.75}O_{3-\delta}$ achieved an energy density of 157 kJ kg_{ABO3}^{-1} under a temperature and oxygen partial pressure swing between 400 °C/0.2 atm O_2 and 1100 °C/0.01 atm O_2. The experimental results supported the

© 2023 The Authors. Advanced Energy Materials published by Wiley-VCH GmbH

16146840, 2023, 18, Downloaded from https://advanced.onlinelibrary.wiley.com/doi/10.1002/aenm.202203833, Wiley Online Library on [17/03/2025]. See the Terms and Conditions (https://onlinelibrary.wiley.com/terms-and-conditions) on Wiley Online Library for rules of use; OA articles are governed by the applicable Creative Commons License

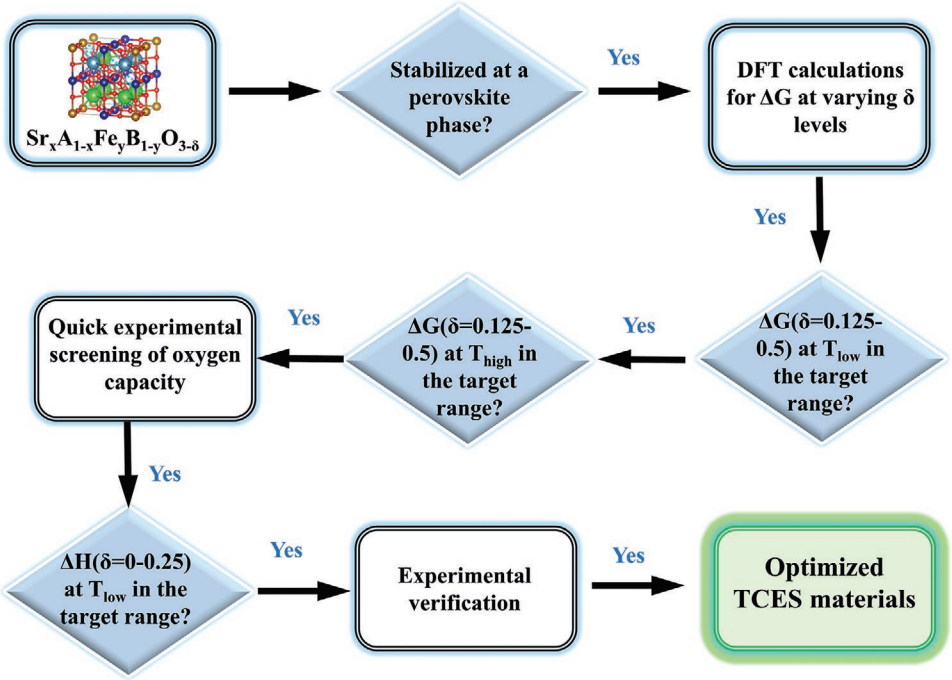

Figure 7. Flowchart for high throughput combinatorial screening of perovskite oxides for TCES.

effectiveness of the high-throughput predictions for oxygen capacity and standard oxidation enthalpy. An improved set of screening criteria was also developed based on the experimental and DFT results. This improved approach, with an average deviation of 25.4% for predicting the standard oxidation enthalpy and a correlation coefficient of –0.64 for predicting the oxygen capacity, would be highly useful for the accelerated development of redox-active perovskite oxides.

4. Experimental Section

DFT Calculations: First-principles DFT simulations were executed using the Vienna ab initio Simulation package software.[82] Here the frozen-core all-electron projector augmented wave model[83] and Perdew–Burke–Ernzerhof functional were utilized.[84] The energy cutoff was set to 450 eV and the force and energy converged with the criteria of 0.01 eV $Å^{-1}$ and 10^{-5} eV, respectively. Gaussian smearing was employed with a width of 0.1 eV for optimization simulation. $1 \times 1 \times 1$ and $1 \times 2 \times 2$ *k*-points were used for the $2 \times 2 \times 2$ $Sr_xA_{1-x}Fe_yB_{1-y}O_{3-\delta}$ perovskite supercells and brownmillerite structures, respectively. Based on previous studies,[85,86] DFT + U method was utilized for *d* orbitals of Fe, Co, Cu, Mn, Ni, and Ti[87] with $U_{eff} = 4$, 3.4, 4, 3.9, 6, and 3 eV, respectively, which have been proven to give reasonable predictions of redox properties in previous works.[85,86] Ferromagnetic phase magnetic ordering was only considered for all the doped structures owing to the negligible effect of magnetic ordering on oxygen vacancy formation and migration.[88] The initial spin moments for Fe, Co, Mn, and Ni were set to 4, 5, 5, and 5, respectively.

A Monte Carlo special quasi-random structures method[89] was applied to determine the positions of all A- and B-site dopants and oxygen vacancies to approach randomly disordered structures. The zero-point energy was calculated using the Phonopy code.[90] For an optimized $Sr_xA_{1-x}Fe_yB_{1-y}O_{3-\delta}$ crystal structure, its dynamical matrix of force constants was obtained by using the forces from DFT calculations on a $2 \times 2 \times 2$ supercell. The enthalpy of O_2 was computed using the complete basis set-quadratic Becke3 method in Gaussian 16.[91] A more detailed description of the simulation approach can be found in the previous publication.[74]

Given an increment of 0.125 for both dopant fraction and nonstoichiometry, 2401 perovskite models and 9604 different conditions were constructed, including various A-site cations (Ca, K, Y, Ba, La, or Sm) and/or B-site cations (Co, Cu, Mn, Mg, Ni, or Ti). Some unstable perovskite structures were excluded by the preliminary screening with two criteria. First, the compositions should be charge neutral, leading to the removal of 168 materials from the screening list. Then, a modified tolerance factor was used to further eliminate high-distortion candidates, leaving 2003 materials for high-throughput calculations of ΔG, ΔH, and ΔS. The total computation time for calculating all 2003 $Sr_xA_{1-x}Fe_yB_{1-y}O_{3-\delta}$ compositions (geometric optimization + free energy calculations) was ≈70 d with 30 nodes (12 cores and 2.9 GHz).

Material Preparation and Characterization: All the perovskite oxides were synthesized using a solid-state method. In a typical synthesis of $Sr_xBa_{1-x}Fe_yMn_{1-y}O_{3-\delta}$, stoichiometric amounts of $SrCO_3$, BaO, Fe_2O_3, and MnO_2 were weighted and put in a 5 mL polytetrafluoroethylene vial. Then, 2 mm ZrO beads were added into the vial with a mass ratio of 5:1. 2 mL ethanol (>99 vol% purity) was further added to the mixture to prevent powders from sticking to the vial walls.[92] Four vials with four different materials were housed in a stainless-steel sample jar and then balled milled with 1200 RPM for 3 or 24 h. Based on the XRD patterns, excessive ball-milling time will cause minor impurities in some materials. The ball milling time was specified in Table S1 in the Supporting Information. The resulting wet mixture in each vial was dried at 95 °C for 0.5 h and 130 °C for 15 min to remove ethanol. The powder mixture was separated from ZrO_2 beads and then fired at 1000 °C in a muffle furnace for 10 h to obtain the perovskite structure. The heating and cooling rates were all set to be 3 °C min^{-1}. Finally, the perovskite samples were sieved to two desired particle size ranges, i.e., 180–250 µm for oxygen release experiments and 0–180 µm for XRD and reaction enthalpy experiments. 61 different materials were synthesized in this study. Precursors used were $SrCO_3$ (>99.9%), $CaCO_3$ (>99.9%), BaO (>98%), La_2O_3 (>99%), Fe_2O_3(>99%), MnO_2(>99%), TiO_2(>99%), and MgO (>99%).

Crystal structures of the samples were determined on an Empyrean PANalytical XRD with Cu-K_α radiation (λ = 1.5406 Å) operating at 45 kV

© 2023 The Authors. Advanced Energy Materials published by Wiley-VCH GmbH

16146840, 2023, 18, Downloaded from https://advanced.onlinelibrary.wiley.com/doi/10.1002/aenm.202203833, Wiley Online Library on [17/03/2025]. See the Terms and Conditions (https://onlinelibrary.wiley.com/terms-and-conditions) on Wiley Online Library for rules of use; OA articles are governed by the applicable Creative Commons License

and 40 mA. The scan was conducted from 2θ of 15° to 80° with a step size of 0.0262° and a hold time of 0.2 s for each step. The XRD phases were identified using Highscore Plus software. As shown in Figure S8 in the Supporting Information, 45 samples were pure perovskite phases or contained negligibly small phase impurities, but the rest of the 16 samples contained notable impurities.

Evaluation of the Redox Properties: Two types of experiments were carried out in a TGA (TA-Instrument, SDT Q650). The oxygen capacity experiments were used as the first-step screening for the above-mentioned 45 samples. In a typical experiment, 40–50 mg samples with a particle size of 180–250 µm were loaded into an Al_2O_3 crucible with a 6.5 mm inner diameter and then placed in the TGA. The total flow rate was maintained at 200 mL min^{-1} and three oxygen concentrations were tested, i.e., 0.2 atm, 0.01 atm, and Ar (Airgas UHP 5.0 grade). The oxygen concentration was varied by mixing pure oxygen (Airgas extra dry grade O_2) with Ar. The oxygen partial pressure in the Ar flow, which was $\approx 5 \times 10-^{5}$ atm, was measured by an oxygen analyzer (Setnag). The sample was increased from room temperature to 180 °C under a 0.2 atm O_2 atmosphere and then was held for 10 min to eliminate moisture. After that, the temperature was ramped to 700 °C and followed by a 10 min isothermal step as a pretreatment. Then, the temperature was decreased to 400 °C and held for 15 min to obtain the first particle weight m_1. Another two points were measured at 800 and 1100 °C, respectively. Afterward, the temperature was ramped back to 400 °C and the oxygen concentration was changed to 1%. The next cycle of the temperature test was started using the same program. A typical testing program is shown in Figure S3 in the Supporting Information. After measuring the particle weights at different temperatures and oxygen concentrations, oxygen capacities were obtained under different conditions. The oxygen release kinetics of the Ba-doped or Ba/Mg codoped $SrFeO_{3-\delta}$ were also tested. Details are provided in the Supporting Information.

Twenty samples with an oxygen capacity >1 wt% were then tested to obtain the oxygen nonstoichiometry and reaction enthalpy. In a typical experiment, ≈30 mg samples with a particle size <180 µm were tested in the TGA. The total flow rate was also maintained at 200 mL min^{-1}, and seven different oxygen concentrations were tested, i.e., 0.8, 0.2, 0.05, 0.01, 0.003, 0.0005 atm O_2, and Ar. The 0.003 and 0.0005 atm oxygen concentrations were realized by mixing 1.048 vol% O_2 calibration gas (balance Ar) with pure Ar. The temperature was first increased to 1100 °C under the 80% O_2 atmosphere and then held for a specific time until the particle weight change reached equilibrium. The temperature was then sequentially decreased in a stepwise mode by 400 °C with an increment of 100 °C. Afterward, the temperature was ramped back to 1100 °C and then the gas atmosphere was switched to 20% O_2. The next cycle of the temperature test was started under a different oxygen concentration using the same program. A typical testing experiment is shown in Figure S9 in the Supporting Information. The calculation methods for thermodynamic properties (δ, ΔH, and ΔS) were elaborated on in the Supporting Information.

Supporting Information

Supporting Information is available from the Wiley Online Library or from the author.

Acknowledgements

R.C., H.B., and X.W. contributed equally to this work. This work was supported by the National Science Foundation (Grant Nos. CBET-2116724 and CBET-1923468) and the North Carolina State University Kenan Institute for Engineering, Technology, and Science. The authors acknowledge the use of the Analytical Instrumentation Facility (AIF) at North Carolina State University, which was supported by the State of North Carolina and the National Science Foundation. The authors would also like to acknowledge the assistance of Jackson Massey in material synthesis and data analysis.

Conflict of Interest

The authors declare no conflict of interest.

Data Availability Statement

The data that support the findings of this study are available from the corresponding author upon reasonable request.

Keywords

energy storage, high-throughput screening, mixed oxides, perovskites, redox

Received: November 11, 2022
Revised: February 17, 2023
Published online: March 22, 2023

[1] T. M. Gür, *Energy Environ. Sci.* **2018**, *11*, 2696.
[2] M. Flores-Granobles, M. Saeys, *Energy Environ. Sci.* **2020**, *13*, 1923.
[3] British Petroleum. BP statistical review of world energy 2022, https://www.bp.com/en/global/corporate/energy-economics/statistical-review-of-world-energy.html (accessed: March 2023).
[4] B. Arias, Y. A. Criado, A. Sanchez-Biezma, J. C. Abanades, *Appl. Energy* **2014**, *132*, 127.
[5] L. M. P. Tumiran, E. Y. P. Sarjiya, *Renewable Energy* **2021**, *163*, 561.
[6] F. Liu, F. Wang, J. Yan, G. Xu, T. Bi, *2020 5th Asia Conf. Power Electr. Eng. (ACPEE)*, Chengdu, China, June **2020**.
[7] G. Airò Farulla, M. Cellura, F. Guarino, M. Ferraro, *Appl. Sci.* **2020**, *10*, 3142.
[8] M. M. Rahman, A. O. Oni, E. Gemechu, A. Kumar, *Energy Convers. Manage.* **2020**, *223*, 113295.
[9] H. Chen, T. N. Cong, W. Yang, C. Tan, Y. Li, Y. Ding, *Prog. Nat. Sci.* **2009**, *19*, 291.
[10] U. Pelay, L. Luo, Y. Fan, D. Stitou, M. Rood, *Renewable Sustainable Energy Rev.* **2017**, *79*, 82.
[11] X. Chen, X. Jin, X. Ling, Y. Wang, *ACS Sustainable Chem. Eng.* **2020**, *8*, 7928.
[12] Y. Wang, S. Lou, Y. Wu, S. Wang, *IEEE Trans. Power Syst.* **2020**, *35*, 1178.
[13] J. Chang, G. Lee, D. Adams, H. Ahn, J. Lee, M. Oh, *Korean J. Chem. Eng.* **2021**, *38*, 1333.
[14] Global Thermal Energy Storage Capacity 2019–2030, https://www.Statista.Com/statistics/1307219/thermal-energy-storage-capacity-global/ (accessed: February 2023).
[15] T. Bauer, N. Pfleger, D. Laing, W.-D. Steinmann, M. Eck, S. Kaesche, *Molten Salts Chemistry*, Elsevier **2013**, pp. 415–438.
[16] S. Bell, T. Steinberg, G. Will, *Renewable Sustainable Energy Rev.* **2019**, *114*, 109328.
[17] Z. Ma, R. Zhang, F. Sawaged, ASME 2017 11th Int. Conf. Energy Sustainability collocated ASME 2017 Power Conf. Joint ICOPE-17, ASME 2017 15th Int. Conf. Fuel Cell Sci., Eng. Technol., ASME 2017 Nuclear Forum, Charlotte, North Carolina, USA, **2017**.
[18] A. Caraballo, S. Galán-Casado, Á. Caballero, S. Serena, *Energies* **2021**, *14*, 1197.
[19] J. S. Prasad, P. Muthukumar, F. Desai, D. N. Basu, M. M. Rahman, *Appl. Energy* **2019**, *254*, 113733.
[20] W. Aftab, A. Usman, J. Shi, K. Yuan, M. Qin, R. Zou, *Energy Environ. Sci.* **2021**, *14*, 4268.
[21] Y. Zhao, C. Y. Zhao, C. N. Markides, H. Wang, W. Li, *Appl. Energy* **2020**, *280*, 115950.

© 2023 The Authors. Advanced Energy Materials published by Wiley-VCH GmbH

16146840, 2023, 18, Downloaded from https://advanced.onlinelibrary.wiley.com/doi/10.1002/aenm.202203833, Wiley Online Library on [17/03/2025]. See the Terms and Conditions (https://onlinelibrary.wiley.com/terms-and-conditions) on Wiley Online Library for rules of use; OA articles are governed by the applicable Creative Commons License

[22] C. Liu, Z. Rao, *Sci. Bull.* **2017**, *62*, 231.
[23] S. Saha, A. R. M. Ruslan, A. K. M. M. Morshed, M. Hasanuzzaman, *Clean Technol. Environ. Policy* **2020**, *23*, 531.
[24] P. Pardo, A. Deydier, Z. Anxionnaz-Minvielle, S. Rougé, M. Cabassud, P. Cognet, *Renewable Sustainable Energy Rev.* **2014**, *32*, 591.
[25] R. Salgado-Pizarro, A. Calderón, A. Svobodova-Sedlackova, A. I. Fernández, C. Barreneche, *J. Energy Storage* **2022**, *51*, 104377.
[26] M. Schmidt, M. Linder, *Front. Energy Res.* **2020**, *8*, 137.
[27] A. A. Hawwash, H. Hassan, M. Ahmed, S. Ookawara, K. E. feky, *Energy Procedia* **2017**, *141*, 310.
[28] Y. Yang, Y. Li, X. Yan, J. Zhao, C. Zhang, *Energies* **2021**, *14*, 6847.
[29] S. Wu, C. Zhou, E. Doroodchi, R. Nellore, B. Moghtaderi, *Energy Convers. Manage.* **2018**, *168*, 421.
[30] L. André, S. Abanades, *Energies* **2020**, *13*, 5859.
[31] M. Saghafifar, M. A. Schnellmann, S. A. Scott, *Appl. Energy* **2020**, *279*, 115553.
[32] M. Saghafifar, S. A. Scott, *Chem. Eng. J.* **2021**, *423*, 128789.
[33] K. Snini, M. Akyol, M. Ellouze, L. El Mir, F. Ghribi, A. Ekicibil, *J. Alloys Compd.* **2021**, *874*, 159866.
[34] J. Dou, E. Krzystowczyk, X. Wang, T. Robbins, L. Ma, X. Liu, F. Li, *ChemSusChem* **2020**, *13*, 385.
[35] E. Bakken, T. Norby, S. Stolen, *Solid State Ionics* **2005**, *176*, 217.
[36] N. Galinsky, M. Sendi, L. Bowers, F. Li, *Appl. Energy* **2016**, *174*, 80.
[37] N. Galinsky, A. Mishra, J. Zhang, F. Li, *Appl. Energy* **2015**, *157*, 358.
[38] Q. Imtiaz, D. Hosseini, C. R. Muller, *Energy Technol.* **2013**, *1*, 633.
[39] B. Bulfin, J. Vieten, D. E. Starr, A. Azarpira, C. Zachäus, M. Hävecker, K. Skorupska, M. Schmücker, M. Roeb, C. Sattler, *J. Mater. Chem. A* **2017**, *5*, 7912.
[40] S. M. Babiniec, E. N. Coker, J. E. Miller, A. Ambrosini, *Int. J. Energy Res.* **2016**, *40*, 280.
[41] L. Imponenti, K. J. Albrecht, R. J. Braun, G. S. Jackson, *ECS Trans.* **2016**, *72*, 11.
[42] L. Imponenti, K. J. Albrecht, J. W. Wands, M. D. Sanders, G. S. Jackson, *Sol. Energy* **2017**, *151*, 1.
[43] E. A. Antipinskaya, B. V. Politov, S. A. Petrova, V. P. Zhukov, E. V. Chulkov, A. Y. Suntsov, V. L. Kozhevnikov, *J. Energy Storage* **2022**, *53*, 105175.
[44] K. J. Albrecht, G. S. Jackson, R. J. Braun, *Appl. Energy* **2016**, *165*, 285.
[45] F. Jin, C. Xu, H. Yu, X. Xia, F. Ye, X. Li, X. Du, Y. Yang, *ACS Appl. Mater. Interfaces* **2021**, *13*, 3856.
[46] E. Mastronardo, X. Qian, J. M. Coronado, S. M. Haile, *J. Energy Storage* **2021**, *40*, 102793.
[47] D. Yilmaz, E. Darwish, H. Leion, *Ind. Eng. Chem. Res.* **2021**, *60*, 1250.
[48] M. Takacs, M. Hoes, M. Caduff, T. Cooper, J. R. Scheffe, A. Steinfeld, *Acta Mater.* **2016**, *103*, 700.
[49] M. Ezbiri, M. Takacs, D. Theiler, R. Michalsky, A. Steinfeld, *J. Mater. Chem. A* **2017**, *5*, 4172.
[50] S. M. Babiniec, E. N. Coker, J. E. Miller, A. Ambrosini, *Sol. Energy* **2015**, *118*, 451.
[51] S. M. Babiniec, E. N. Coker, A. Ambrosini, J. E. Miller, *AIP Conf. Proc.* **2016**, *1734*, 050006.
[52] N. Gokon, T. Yawata, S. Bellan, T. Kodama, H.-S. Cho, *Energy* **2019**, *171*, 971.
[53] R. H. Görke, E. J. Marek, F. Donat, S. A. Scott, *Int. J. Greenhouse Gas Control* **2020**, *94*, 102891.
[54] C. Y. Lau, M. T. Dunstan, W. Hu, C. P. Grey, S. A. Scott, *Energy Environ. Sci.* **2017**, *10*, 818.
[55] E. Krzystowczyk, X. Wang, J. Dou, V. Haribal, F. Li, *Phys. Chem. Chem. Phys.* **2020**, *22*, 8924.
[56] X. Chen, M. Kubota, S. Yamashita, H. Kita, *J. Energy Storage* **2021**, *38*, 102501.
[57] J. Vieten, B. Bulfin, M. Senholdt, M. Roeb, C. Sattler, M. Schmücker, *Solid State Ionics* **2017**, *308*, 149.
[58] E. Darwish, M. Mansouri, D. Yilmaz, H. Leion, *Processes* **2021**, *9*, 1817.
[59] P. Yuan, H. Xu, Z. Ning, G. Xiao, *J. Energy Storage* **2023**, *61*, 106695.
[60] E. Mastronardo, X. Qian, J. M. Coronado, S. M. Haile, *J. Mater. Chem. A* **2020**, *8*, 8503.
[61] Z. Zhang, L. Andre, S. Abanades, *Sol. Energy* **2016**, *134*, 494.
[62] E. J. Popczun, D. N. Tafen, S. Natesakhawat, C. M. Marin, T.-D. Nguyen-Phan, Y. Zhou, D. Alfonso, J. W. Lekse, *J. Mater. Chem. A* **2020**, *8*, 2602.
[63] T. Jia, E. J. Popczun, J. W. Lekse, Y. Duan, *Phys. Chem. Chem. Phys.* **2020**, *22*, 16721.
[64] X. Wang, E. Krzystowczyk, J. Dou, F. Li, *Chem. Mater.* **2021**, *33*, 2446.
[65] A. A. Emery, C. Wolverton, *Sci. Data* **2017**, *4*, 170153.
[66] R. B. Wexler, G. S. Gautam, E. B. Stechel, E. A. Carter, *J. Am. Chem. Soc.* **2021**, *143*, 13212.
[67] T. Jia, E. J. Popczun, J. W. Lekse, Y. Duan, *Appl. Energy* **2021**, *281*, 116040.
[68] D. Gryaznov, M. W. Finnis, R. A. Evarestov, J. Maier, *Solid State Ionics* **2014**, *254*, 11.
[69] J. Vieten, B. Bulfin, P. Huck, M. Horton, D. Guban, L. Zhu, Y. Lu, K. A. Persson, M. Roeb, C. Sattler, *Energy Environ. Sci.* **2019**, *12*, 1369.
[70] Z. Yang, Y. Lin, *Solid State Ionics* **2005**, *176*, 89.
[71] J. Fan, W. Li, S. Li, J. Yang, *Adv. Sci.* **2022**, *9*, 2202811.
[72] M. M. Nair, S. Abanades, *Sustainable Energy Fuels* **2018**, *2*, 843.
[73] C. J. Bartel, C. Sutton, B. R. Goldsmith, R. Ouyang, C. B. Musgrave, L. M. Ghiringhelli, M. Scheffler, *Sci. Adv.* **2019**, *5*, eaav0693.
[74] X. Wang, Y. Gao, E. Krzystowczyk, S. Iftikhar, J. Dou, R. Cai, H. Wang, C. Ruan, S. Ye, F. Li, *Energy Environ. Sci.* **2022**, *15*, 1512.
[75] A. Benato, A. Stoppato, *J. Energy Storage* **2018**, *17*, 29.
[76] E. Krzystowczyk, V. Haribal, J. Dou, F. Li, *ACS Sustainable Chem. Eng.* **2021**, *9*, 12185.
[77] H. E. Bush, N. P. Nguyen, T. Farr, P. G. Loutzenhiser, A. Ambrosini, *Solid State Ionics* **2021**, *368*, 115692.
[78] A. Jun, S. Yoo, O. Gwon, J. Shin, G. Kim, *Electrochim. Acta* **2013**, *89*, 372.
[79] G. Luongo, F. Donat, C. R. Muller, *Phys. Chem. Chem. Phys.* **2020**, *22*, 9272.
[80] B. Bulfin, J. Lapp, S. Richter, D. Gubàn, J. Vieten, S. Brendelberger, M. Roeb, C. Sattler, *Chem. Eng. Sci.* **2019**, *203*, 68.
[81] T. P. Farr, N. P. Nguyen, E. Bush, A. Ambrosini, P. G. Loutzenhiser, *Materials (Basel)* **2020**, *13*, 5123.
[82] G. Kresse, J. Furthmuller, *Phys. Rev. B: Condens. Matter* **1996**, *54*, 11169.
[83] P. E. Blochl, *Phys. Rev. B: Condens. Matter* **1994**, *50*, 17953.
[84] J. P. Perdew, K. Burke, M. Ernzerhof, *Phys. Rev. Lett.* **1996**, *77*, 3865.
[85] A. Jain, G. Hautier, C. J. Moore, S. P. Ong, C. C. Fischer, T. Mueller, K. A. Persson, G. Ceder, *Comput. Mater. Sci.* **2011**, *50*, 2295.
[86] G. Hautier, S. P. Ong, A. Jain, C. J. Moore, G. Ceder, *Phys. Rev. B* **2012**, *85*, 155208.
[87] V. V. Anisimov, J. Zaanen, O. K. Andersen, *Phys. Rev. B: Condens. Matter* **1991**, *44*, 943.
[88] Y. L. Lee, J. Kleis, J. Rossmeisl, D. Morgan, *Phys. Rev. B: Condens. Matter Mater. Phys.* **2009**, *80*, 308.
[89] R. P. Stoffel, C. Wessel, M. W. Lumey, R. Dronskowski, *Angew. Chem., Int. Ed. Engl.* **2010**, *49*, 5242.
[90] A. Togo, I. Tanaka, *Scr. Mater.* **2015**, *108*, 1.
[91] M. J. Frisch, G. W. Trucks, H. B. Schlegel, G. E. Scuseria, M. A. Robb, J. R. Cheeseman, G. Scalmani, V. Barone, G. A. Petersson, H. Nakatsuji, *Gaussian 16, Revision C.01*, Gaussian Inc., Wallingford, CT, USA, **2016**.
[92] Ž. Kesić, I. Lukić, M. Zdujić, Č. Jovalekić, V. Veljković, D. Skala, *Fuel Process. Technol.* **2016**, *143*, 162.

© 2023 The Authors. Advanced Energy Materials published by Wiley-VCH GmbH

16146840, 2023, 18, Downloaded from https://advanced.onlinelibrary.wiley.com/doi/10.1002/aenm.202203833, Wiley Online Library on [17/03/2025]. See the Terms and Conditions (https://onlinelibrary.wiley.com/terms-and-conditions) on Wiley Online Library for rules of use; OA articles are governed by the applicable Creative Commons License